

# Massive Growth of Graphene Quartz Fiber as a Multifunctional Electrode

Guang Cui,<sup>1</sup> Yi Cheng,<sup>1</sup> Can Liu,<sup>1</sup> Kewen Huang, Junliang Li, Puxin Wang, Xiaojie Duan, Ke Chen,\* Kaihui Liu,\* and Zhongfan Liu\*



Cite This: <https://dx.doi.org/10.1021/acsnano.0c01298>



Read Online

ACCESS |



Metrics & More



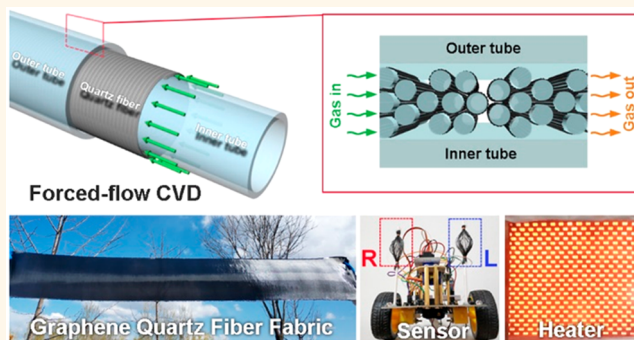
Article Recommendations



Supporting Information

**ABSTRACT:** Quartz fiber, a widely used reinforcer with high tensile strength and excellent heat resistance, can have more attractive electrical applications such as electromagnetic interference shielding, static dissipation, and strain sensing if it becomes conductive. Many attempts have been made to increase the electrical conductivity of quartz fiber by surface coating of conductive polymers or plating of metal films, but suffers from sacrificing flexibility and causing heavy metal pollution. Here we designed and massively produced a hybrid structure of graphene quartz fiber (GQF) by a forced-flow chemical vapor deposition (CVD) method, which combines the excellent conductivity of graphene and the extraordinary properties of quartz fiber. The as-fabricated flexible GQF exhibited high sensitivity, fast response (<0.5 s) and good durability (~5000 cycles) to organic solvent vapor, suitable as a real-time biomimetic gas sensor. Furthermore, the massively produced GQFs can be knitted into meter-scale fabrics with tunable conductivity (sheet resistances of 0.2–10 kΩ/sq) and superior electrothermal conversion efficiency (up to 980 °C within a few seconds at 24 V), thus propelling its promising application in industrial electric heaters. We expect this hybrid GQF material will greatly expand the applications of traditional quartz fiber into an infusive multifunctional regime.

**KEYWORDS:** graphene, quartz fiber, forced-flow chemical vapor deposition, biomimetic sensor, electrothermal heater



Graphene, an atomically thin two-dimensional material with honeycomb structure, has stimulated enormous interest owing to its excellent mechanical, electrical, optical, and thermal properties.<sup>1–6</sup> These excellent properties of graphene make it an important building block to realize a wide range of applications in electronics, optoelectronics, and photovoltaics.<sup>7–9</sup> In fact, beyond the advances to device miniaturization, rich graphene-based macroscopic structures, such as three-dimensional aerogels, two-dimensional membranes, and one-dimensional fibers, have also displayed extensive applications in the fields of energy storage, sensing, catalyst, and engineering materials.<sup>10–12</sup> Among them, graphene fiber exhibits superior electrical and thermal properties and is also compatible with flexible electronics, which boosts the large-scale application of macroscopic graphene composites.<sup>13–16</sup>

However, as for the assembly of graphene fiber, the intrinsic properties of graphene degenerate dramatically due to the microscopic structural damage inevitably involved in the fabrication process.<sup>17–19</sup> Currently, the prevailing method for graphene fiber assembly is solution spinning, in which graphene oxide (GO) liquid crystals are injected into a coagulation bath to form a GO fiber. After that, a reducing treatment with chemical

species such as HI, N<sub>2</sub>H<sub>4</sub>·H<sub>2</sub>O, and NaBH<sub>4</sub> is enormously needed to remove the oxygen functional groups.<sup>20,21</sup> It has been proved that the thermal and electrical conductivities of the GO-derived graphene fibers are incomparable to that of chemical vapor deposition (CVD)-grown graphene due to the enhanced scattering of phonons and electrons in randomly distributed micrometer-scale graphene flakes with enormous defects, folds, and functional groups.<sup>22,23</sup> Therefore, it is in great demand to develop a practical way for scalable production of graphene fibers without sacrificing the high quality of pristine graphene.

In this work, we utilize the traditional quartz fiber as the supporting substrate to fabricate a high-quality graphene quartz fiber by a direct forced-flow CVD growth strategy, which combines the excellent electrical conductivity of CVD graphene

**Received:** February 17, 2020

**Accepted:** April 22, 2020

**Published:** April 22, 2020

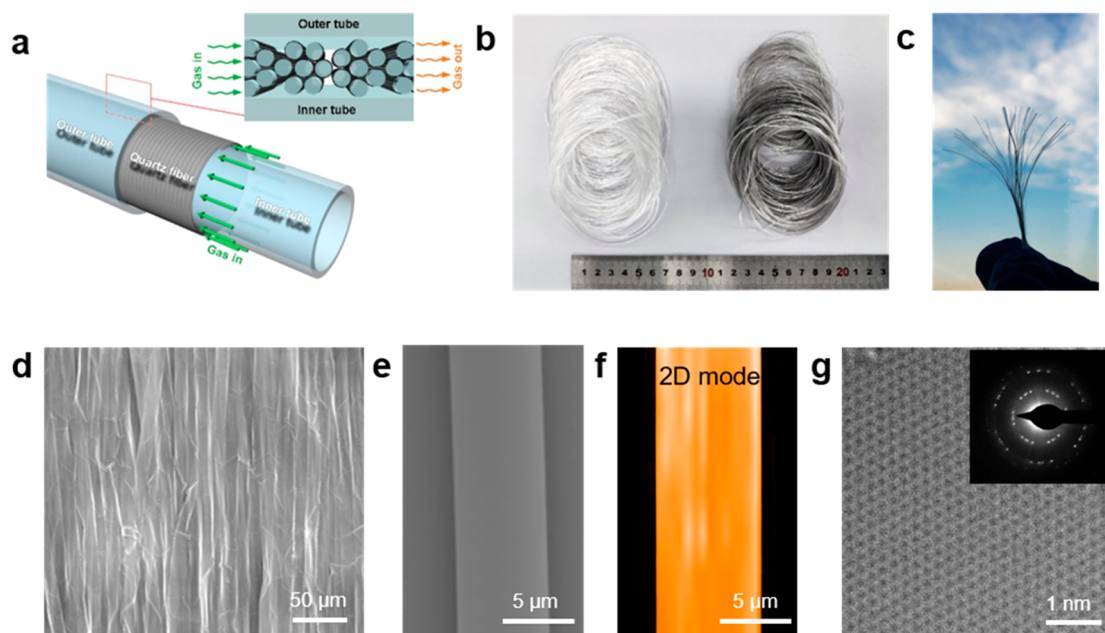


**Figure 1.** Fabrication of GQF by the forced-flow CVD method. (a) Schematic of the experimental design. The quartz fiber was coiled on the surface of an inner tube and then encapsulated into an outer tube. (b) 50-m-long quartz fiber bundle before (left) and after (right) graphene growth. (c) Details of a GQF bundle with thousands of monofilaments. (d, e) SEM images of a bundle of graphene ribbons (d) and each graphene ribbon (e) after etching the core quartz fiber. (f, g) 2D-mode Raman intensity mapping (f), AC-TEM image (g), and the corresponding SAED pattern (inset) in (g).

and the good flexibility of quartz fiber,<sup>24,25</sup> proven to be a feasible solution to modulate the conductivity of quartz fiber as well. With such a material-growth design, a continuous and uniform graphene film on the quartz fiber surface is obtained without the aid of any metal catalysts, while avoiding the coke accumulation and quartz-fiber embrittlement problems in the traditional atmospheric-pressure chemical vapor deposition (APCVD) process.<sup>26–29</sup> The as-fabricated graphene quartz fiber (GQF), with prominent electrical conductivity and high flexibility, exhibits high sensitivity and good durability to flammable gas when incorporated with a smart robot as a biomimetic gas sensor. Furthermore, the GQF can be knitted into a flexible and electrically tunable fabric, promoting the emerging ultrafast high-temperature graphene electrothermal heater.

## RESULTS AND DISCUSSION

A 50-m-long quartz fiber bundle was coiled on the surface of a quartz tube for graphene growth. In general, for the metal-catalyst-free growth of graphene *via* pyrolysis, the adequate concentration and effective molecular collision of active carbon feedstock are crucial for graphene nucleation and edge attachment at high temperature. To accelerate this reaction, we have designed a narrow space to produce the forced flow of carbon feedstock at low pressure by using another coaxial quartz tube as a tight sleeve for the coiled quartz fiber bundle, as shown in Figure 1a. When the reactant gas was pumped into the gap between the two quartz tubes, the active carbon species would diffuse into the narrow space ( $\sim 200$  nm, Figure S1) among the GQF monofilaments, experiencing a relatively frequent collision among the fiber surfaces for graphene nucleation and growth (see Experimental Section for details). The darker optical contrast of as-fabricated GQF (Figure 1b) reveals the successful growth of graphene on the quartz fiber surface. In fact, the quartz fiber bundle contains thousands of monofilaments with a

diameter of *ca.* 6  $\mu\text{m}$ , and the uniform contrast of each graphene-coated monofilament in return reveals the homogeneous carbon feedstock during such a forced-flow CVD process (Figure 1c and Figure S2). The scanning electron microscopic (SEM) image shows the graphene domain size of  $\sim 100$  nm for the GQF (Figure S3a), consistent with that of graphene directly grown on  $\text{SiO}_2$  substrates.<sup>30–32</sup> Further X-ray photoelectron spectroscopy (XPS) measurement of the GQF shows a dominant  $\text{sp}^2$ -carbon-related C 1s peak (284.8 eV), a C–H related peak (285.4 eV), and broad C–O related peaks (Figure S3b), indicating high purity of the graphene coating on quartz fiber.

In order to evaluate the quality of the graphene coating, we etched a core quartz fiber with hydrofluoric acid to leave the graphene shell, which then collapsed into a bundle of overlapped graphene ribbons (Figure 1d,e). Representative Raman mapping exhibits a sharp 2D peak, revealing the high crystallinity of the as-fabricated graphene coating (Figure 1f). Besides, the aberration-corrected transmission electron microscope (AC-TEM) was also applied to show the atomic lattice of an individual graphene domain (Figure 1g). The selected-area electron diffraction (SAED) pattern (aperture size of 200 nm) reveals the polycrystalline structure of the graphene coating on the quartz fiber (Figure 1g inset).

In the typical APCVD process, active carbon species for graphene nucleation and growth accumulate with gradient distribution along the flow direction, especially at the downstream, where the yield of high-concentration carbon species leads to the noncontrollability of the as-grown graphene layer thickness.<sup>27,29,32</sup> As shown at the top of Figure 2a, the nonuniform optical contrast of GQF from left (upstream) to right (downstream) results from the gradient accumulation of carbon layers. The obvious variation of the  $I_{2\text{D}}/I_{\text{G}}$  ratio along the fiber coil (Figure 2b, upper panel), as denoted by triangles of different colors in Figure 2a, also indicates the thickness increment of the APCVD-grown graphene coating. Meanwhile,

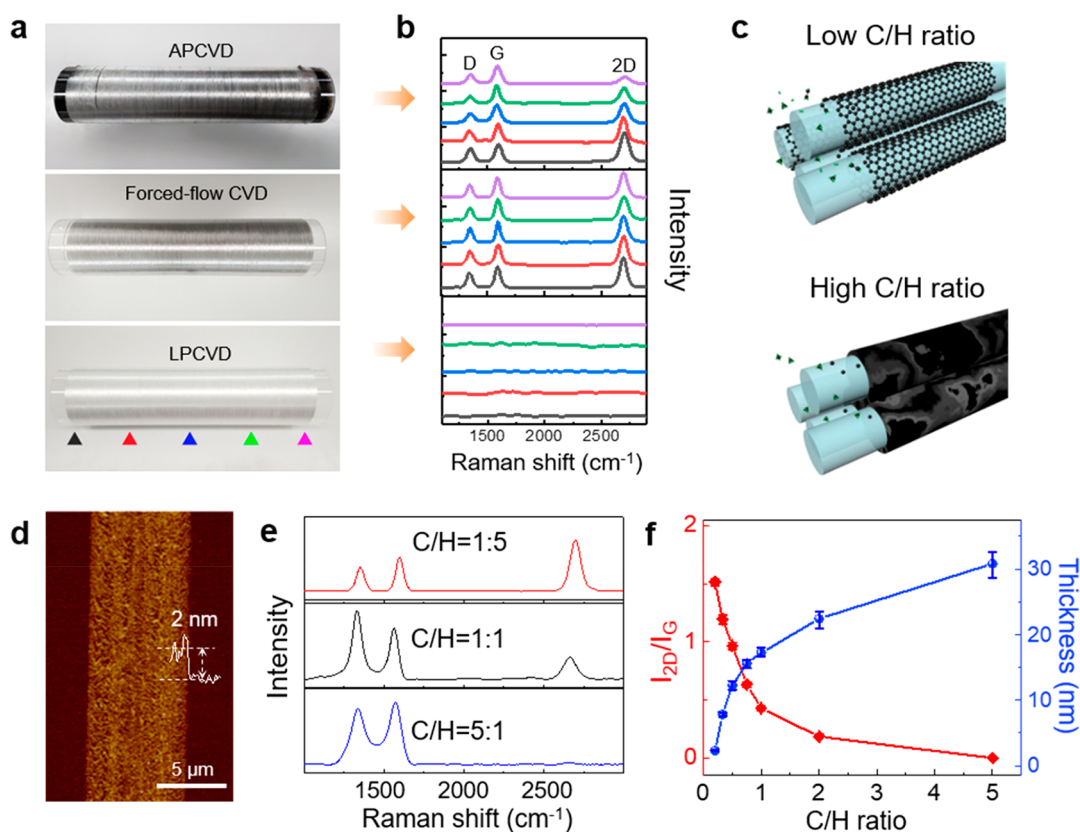


**Figure 2.** GQF obtained by different CVD parameters. (a) As-grown GQF coiled on an inner tube by APCVD (top), forced-flow CVD (middle), and LPCVD (bottom) method. The uniform optical contrast of GQF initially demonstrates the validity of the forced-flow CVD method. (b) Raman spectra of graphene on quartz fiber obtained by APCVD (top), forced-flow CVD (middle), and LPCVD (bottom), respectively, which further confirms the effective and uniform carbon supply for forced-flow CVD. (c) Schematic of the role of the methane/hydrogen ratio in the GQF synthesis. (d) AFM image of a graphene ribbon with a thickness of 2 nm after etching a quartz fiber. (e) Representative Raman spectra of graphene with different methane/hydrogen ratios. (f) Statistics of  $I_{2D}/I_G$  and the corresponding thickness of graphene with the change of the methane/hydrogen ratio.

the relatively high-concentration oxygen and hydroxyl radicals significantly accelerated the microcracking of quartz fiber at high temperature.<sup>33,34</sup> Fortunately, distinct from the APCVD condition, the high-efficiency mass-transport process at low pressure is facile for the more uniform distribution of carbon species.<sup>26</sup> However, the low pyrolysis efficiency of methane in most LPCVD systems<sup>30,31</sup> impedes graphene deposition on quartz fiber in the absence of metal catalysts, because of the lack of sufficient decomposition and an essential amount of carbon feedstocks for graphene nucleation (see Raman spectroscopy analysis in Figure 2b, lower panel). Therefore, in our designed forced-flow CVD process at low pressure, sufficient-concentration methane was forced into the narrow space among thousands of GQF monofilaments, thus yielding a higher collision probability of carbon species to accelerate their decomposition, nucleation, and edge attachment for graphene growth. Such uniformly grown graphene on the fiber surface can be confirmed by the Raman spectra, showing homogeneous  $I_{2D}/I_G$  ratios along the fiber axis (Figure 2b, middle panel).

Meanwhile, by controlling the methane/hydrogen ratio, graphene with one or two layers can be coated on quartz fiber, as confirmed by atomic force microscope (AFM) measurement (Figure 2d). Note that the interlayer distance of these wet-etched ribbons is relatively larger ( $\sim 1.0$  nm) than the empirical height of monolayer graphene on  $\text{SiO}_2/\text{Si}$  substrates ( $\sim 0.7$  nm), due to the graphene wrinkle formation and water molecule intercalation between overlapped graphene layers. In principal,

the adequate hydrogen supply in such a CVD system plays a critical role in improving the quality of the graphene coating, significantly distinct from the thermal-gradient chemical vapor infiltration (CVI) for the densification of porous carbon-carbon composites.<sup>35–37</sup> To unveil the role of hydrogen in GQF synthesis, the methane/hydrogen ratio is further modulated in the forced-flow CVD system while other parameters maintain constant. With the increase of the methane/hydrogen ratio, the  $I_{2D}/I_G$  ratio in the Raman spectra of samples gradually decreases until the 2D peak disappears (Figure 2f,g). The variations indicate that the as-grown carbon layers under these conditions become much thicker and uneven, in accordance with the SEM observations (Figure S4). The excessive active carbon species ( $\text{CH}_2$ ,  $\text{CH}_3$ , etc.) can be generated at an unreasonably high methane/hydrogen ratio, which are much more likely to aggregate into amorphous carbon particles on the fiber surface. Therefore, we adopt a methane/hydrogen ratio of 1:5 to guarantee a relatively high quality of GQF for further demonstrations.

To explore the applications of the GQF, a bundle of GQFs with a delicate villiform structure, inspired by an insect's antenna, was integrated as a biomimetic gas sensor to control a smart robot (Figure 3a; see Experimental Section), since graphene is of high sensitivity and adsorption capacity to organic molecules as demonstrated by previous research.<sup>38,39</sup> For the detection of acetone vapor, a carrier gas (argon) was introduced into acetone solvent to generate a concentration-

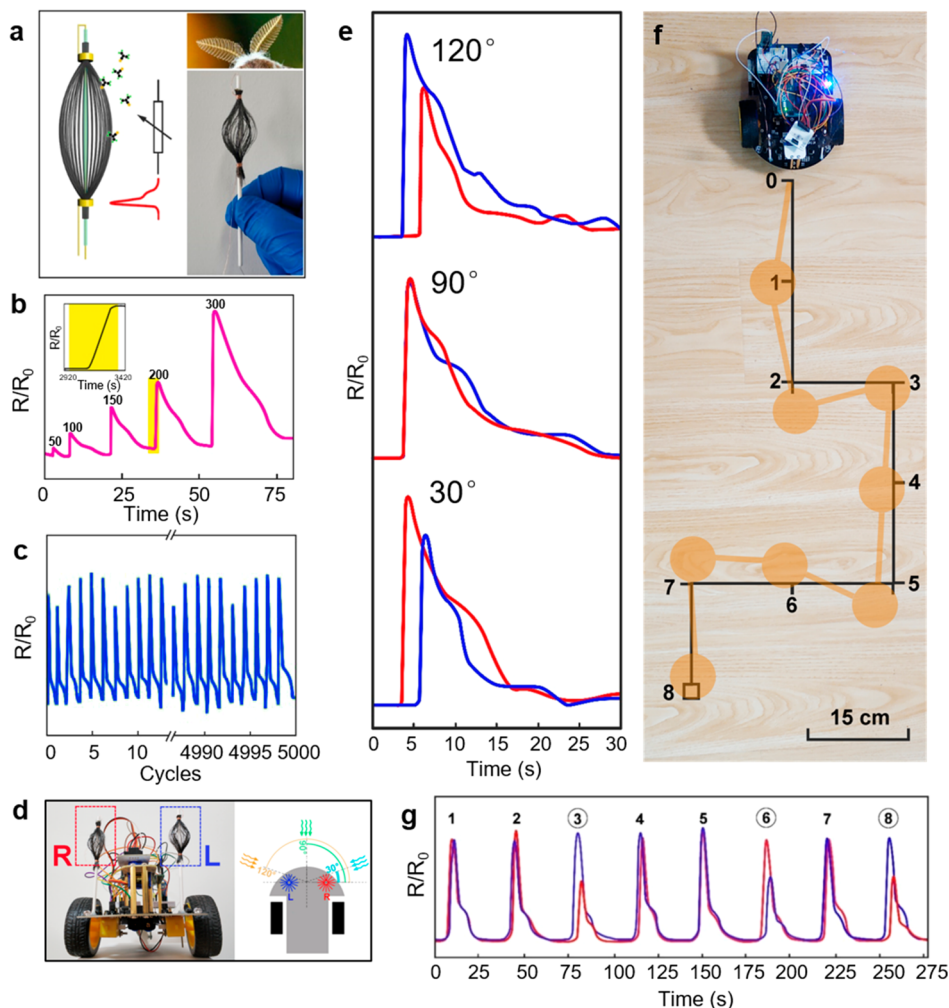


**Figure 3.** Biomimetic vapor sensors based on GQF. (a) Schematic (left) and optical image (right) of the biomimetic GQF sensors. (b) Resistance variation in response to acetone vapor under different carrier gas flow rates from 50 to 300 sccm. The inset shows the zoom-in  $\Delta R/R_0-t$  response curves. (c) Response signal over 5000 cycles under 150 sccm Ar flow. (d) Left (L) and right (R) GQF sensors attached to a mobile robot (left) and the schematic of orientation of the acetone vapor source (right). (e) Response signal variations of R-sensor (red) and L-sensor (blue) at different release directions of acetone vapor. (f) Moving trace of mobile robot (orange line) in response to acetone vapor with a given moving trace (black line). The Arabic numbers refer to the positions where the vapor source moves step by step. (g) Response signal variations of R-sensor (red) and L-sensor (blue) during the movement of the mobile robot.

adjustable acetone vapor by varying the argon flow rate from 50 sccm to 300 sccm (Figure 3b and Figure S6). The signal response of the GQF sensor ( $\Delta R/R_0$  value) can be changed stepwise with a fast response time of less than 0.5 s (Figure 3b inset) under a low driving voltage of 0.5 V, indicating a high sensitivity to acetone vapor. Meanwhile, the GQF sensor shows a long circling stability over 5000 cycles (Figure 3c) with an inconspicuous  $\Delta R/R_0$  variation of less than 10% under ambient environment. Besides acetone molecules, this antenna-like GQF sensor can also exhibit high sensitivity to various organic molecules (Figure S5).

In addition to detecting the vapor origination, the biomimetic GQF sensor can be further implemented with a mobile robot to realize the real-time monitoring of the position of a vapor source like a live insect. As shown in Figure 3d, a pair of GQF sensors as right (R-) and left (L-) “antenna” can give a separated response depending on the direction and position of the acetone vapor source, respectively. As shown in Figure 3e, the R-sensor has a shorter distance from the vapor source compared to the L-sensor, at the vapor direction of  $30^\circ$ , releasing a faster and more

intense response signal. At the middle direction of  $90^\circ$ , the equal distances from the vapor source to each sensor result in identical values of  $\Delta R/R_0$ . Analogously, at the vapor direction of  $120^\circ$ , the faster response signal of the L-sensor is more intense than that of the R-sensor. By analyzing the difference of response signals of the R- and L-sensors, the “insect” (mobile robot) can automatically identify the position of the vapor source and proceed with a tracing movement (Figure 3f and Video S1). Variations of  $\Delta R/R_0$  values of R- and L-sensors at each set position (labeled in Arabic numbers) are also synchronized with the movement of the robot (Figure 3g). Like a real insect, the intelligent robot can also make a high-sensitivity, fast, and stable response to a target.

Besides, the as-fabricated GQF, combining the advantages of graphene and quartz fiber, shows a promising potential in the application of thermal management, since carbon-based materials are attractive for stable electrothermal heaters due to their superior electrothermal conversion efficiency.<sup>40,41</sup> Intriguingly, a uniform GQF fabric (GQFF) with a size of  $40\text{ cm} \times 200\text{ cm}$  can be knitted from the GQF (Figure 4a–c) to fulfill the

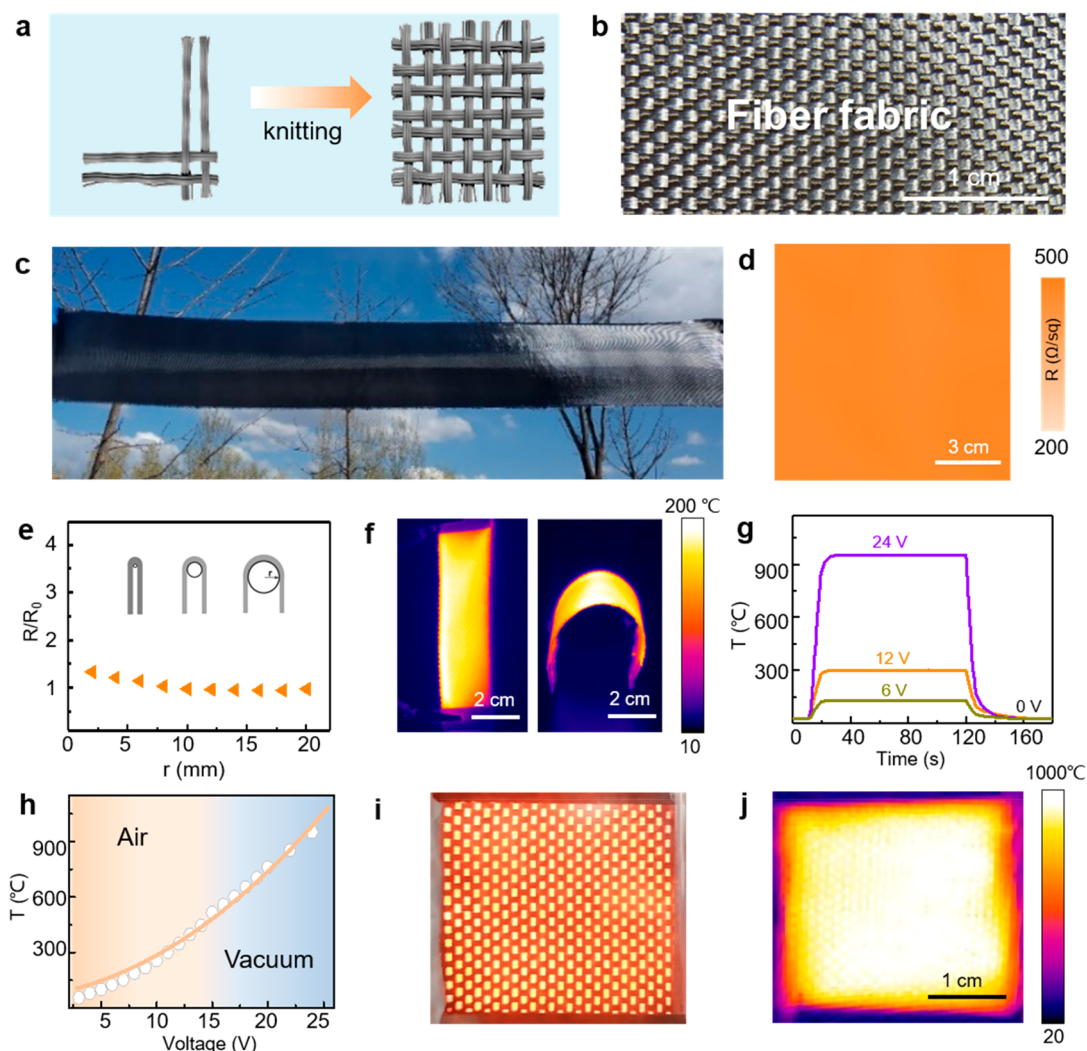


**Figure 4.** Electrothermal devices based on the further-weaved GQFF. (a) Schematic of the knitting process of GQFF. (b) Texture of as-weaved GQFF. (c) 40 cm × 200 cm GQF fabric. (d) Sheet resistance mapping of the GQFF (collected from 11 × 11 points). (e) Bending test of the GQFF (bending for 100 times). (f) Infrared images of a 1.8 cm × 5 cm bent GQFF heater under a voltage of 10 V. (g) Time-dependent temperature variation of GQFF under different voltages. (h) Electrothermal temperature of GQFF under different voltages. (i, j) Optical (i) and infrared (j) images of the GQFF heater under vacuum at an applied voltage of 24 V.

requirements for massive practical applications. By controlling the growth time of graphene on quartz fiber, the sheet resistance of as-weaved GQF fabrics can be tuned with the graphene layer thickness in the range of 0.2–10 kΩ/sq (Figure 4d and Figure S7). Besides, the as-fabricated GQFF also presents great flexibility and durability: negligible changes of sheet resistance at a bending radius from 20 mm to 2 mm (Figure 4e) as well as the uniform distribution of the electrothermal temperature under deformation (curvature radius of ~2 cm, Figure 4f).

Furthermore, we investigated the electrothermal properties of GQFFs. The heating efficiency of GQFFs can be evaluated by time-dependent temperature variation (Figure 4g). When a certain input voltage is applied, the temperature of the GQFF increases to a steady value within 10 s. The response time is defined as the time required to reach 90% of the steady-state temperature. Nonetheless, as the input voltage rises above 15 V, the temperature of the GQFF heater increases slowly due to the serious heat dissipation in air, and the fabric begins to glow and irreversibly oxidize, consistent with the thermogravimetric result of the etched GQFs (Figure S8). Surprisingly, a broad electrothermal temperature range (55 to 980 °C) of the

GQFF heater in a vacuum tube can be achieved by increasing the input voltage from 3 V to 24 V (Figure 4h–j, Video S2). It is worth mentioning that such a high-temperature GQFF heating electrode with low energy consumption has a great potential toward versatile industrial applications, such as quartz tube self-heaters and deicing blades. In addition, the GQFF also possesses hydrophobic and antibacterial properties. On the surface of the GQFF, no *E. coli* colonies were observed, while numerous *E. coli* colonies grew in agar medium at 37 °C beyond the GQFF (Figure S9).

## CONCLUSION

In conclusion, we have designed and prepared a hybrid GQF by a forced-flow CVD method, combining the excellent electrical performance of graphene with the mechanical flexibility of quartz fiber. The high electrical conductivity, preeminent adsorption capacity, and subtle structure make the GQF a promising candidate for real-time gas detection. Furthermore, by the merits of the flexibility of graphene and the high strength of quartz fiber, the as-fabricated GQFs can be weaved into a square-meter-scale GQFF with tunable sheet resistances. The

GQFF exhibits remarkable electrothermal properties with a short response time and an ultrahigh heating temperature, based on its electrothermal conversion efficiency. This work provides not only a multifunctional graphene fiber material but also research on the combination of traditional and frontier materials, which will facilitate the industrialization and commercialization of graphene and quartz fiber in the near future.

## EXPERIMENTAL SECTION

**Forced-Flow CVD Growth of GQF.** A polymer-removed quartz fiber bundle was coiled on the surface of a quartz tube with an outer diameter of about 2.9 in. and was sleeved into the coaxial quartz tube (3.0 in. in inner diameter) of a three-zone high-temperature furnace (Lindberg/Blue). The CVD chamber was flushed with 300 sccm Ar and 50 sccm H<sub>2</sub> under a low pressure of ~100 Pa and heated to the desired growth temperature of 1050 °C. For the growth of graphene, 10–50 sccm methane was pumped into the chamber for 2–4 h. After the growth, methane was stopped and the sample was naturally cooled inside the furnace to room temperature.

**LPCVD Growth of GQF.** A coiled fiber bundle on the quartz tube (2.9 in. in outer diameter) was loaded into the quartz tube (6.0 in. in inner diameter) of a three-zone high-temperature furnace (Lindberg/Blue), and the growth condition was the same as the forced-flow LPCVD process.

**APCVD Growth of GQF.** A coiled fiber bundle on the quartz tube (2.9 in. in outer diameter) was loaded into the quartz tube (3.0 in. in inner diameter) of a three-zone high-temperature furnace (Lindberg/Blue). Prior to heating, the CVD chamber was flushed with 500 sccm of Ar to remove air. Typical growth conditions were 300 sccm of Ar, 50 sccm of H<sub>2</sub>, and 10–50 sccm of CH<sub>4</sub> at 1050 °C for 2 h.

**Transfer Process.** GQF with a 5 mm length was diffused in HF solution (20%) for hours to remove its inner quartz fiber. Afterward, the GQF collapsed into graphene ribbons and then was washed by deionized water and ethanol three times, respectively, to remove the residual chemical reagents. Finally, the graphene ribbons were loaded on the TEM grid by the dipping method.

**Fabrication of the GQF Sensor.** A 3 cm GQF bundle was dispersed and attached to a hollow stick parallelly, while both sides were fixed using copper wires.

**Mobile Robot Tracing Test.** An acetone vapor source, the concentration of which can be modulated by varying the introduced argon flow rate, was initially placed at point 1 (Figure 4f). When 150 sccm of argon, controlled by a gas flowmeter, was introduced to the acetone vapor generation device (Figure S5), the mobile robot would change its orientation to the vapor source and then move forward. In the meantime, the source was moved to the next set point (point 2). This process was repeated eight times, while the mobile robot synchronously moved stepwise along these set points, labeled in Arabic numbers, and finally arrived at the destination (point 8).

**Fabrication of GQF Fabric-Based Electrothermal Devices.** The GQF fabric was knitted using an as-fabricated GQF bundle by a self-built hand loom, the size of which can be adjusted based on further demand. For the GQF-based electrothermal device, two copper electrodes were fixed on both sides of the fabric and the voltage was recorded by a Keithley 2001 multimeter, while the IR image of the GQFF heater was detected by a Fluke Ti 10 infrared camera.

**Bending Test.** A 10 cm × 30 cm GQF fabric was suspended on a 20 cm long quartz cylinder with different diameters in the state of natural ptosis for 200 times with a frequency sweeping of 1 Hz. The sheet resistance of the GQFF bending area was measured before and after the bending test.

**Antibacterial Test.** The spread plate method was used to coculture *Escherichia coli* and GQF in a standard Luria–Bertani solid medium for 24 h at 37 °C.

**Characterization.** The samples were characterized using optical microscopy (Olympus DX51), SEM (Hitachi S-4800, operating at 1 kV), Raman spectroscopy (Horiba, LabRAM HR-800, 514 nm laser excitation, 100× objective lens), XPS (Kratos Analytical Axis-Ultra

spectrometer using a monochromatic Al K $\alpha$  X-ray source), AC-TEM (FEI Titan Themis G2 300, 80 kV), and a Keithley 2001 multimeter (Tektronix, Inc.).

## ASSOCIATED CONTENT

### Supporting Information

The Supporting Information is available free of charge at <https://pubs.acs.org/doi/10.1021/acsnano.0c01298>.

GQF and its fabric characterizations, their properties, and schematic diagrams (PDF)

Video 1: Moving trace of the GQF-based mobile robot following the movement of the acetone vapor source (MP4)

Video 2: Electrothermal heating process of GQF fabrics with an input voltage of 24 V (MP4)

## AUTHOR INFORMATION

### Corresponding Authors

**Ke Chen** – Beijing Graphene Institute (BGI), Beijing 100095, China; Physics Research Center for Two-Dimensional Optoelectronic Materials and Devices, School of Physics and Electronics, Henan University, Kaifeng 475004, China; [orcid.org/0000-0003-2384-8437](https://orcid.org/0000-0003-2384-8437); Email: [kchen@henu.edu.cn](mailto:kchen@henu.edu.cn)

**Kaihui Liu** – Beijing Graphene Institute (BGI), Beijing 100095, China; State Key Laboratory for Mesoscopic Physics, Academy for Advanced Interdisciplinary Studies, School of Physics, Peking University, Beijing 100871, China; [orcid.org/0000-0002-8781-2495](https://orcid.org/0000-0002-8781-2495); Email: [khliu@pku.edu.cn](mailto:khliu@pku.edu.cn)

**Zhongfan Liu** – Center for Nanochemistry, Beijing Science and Engineering Center for Nanocarbons, Beijing National Laboratory for Molecular Sciences, College of Chemistry and Molecular Engineering, Peking University, Beijing 100871, China; Beijing Graphene Institute (BGI), Beijing 100095, China; [orcid.org/0000-0003-0065-7988](https://orcid.org/0000-0003-0065-7988); Email: [zfliu@pku.edu.cn](mailto:zfliu@pku.edu.cn)

### Authors

**Guang Cui** – Center for Nanochemistry, Beijing Science and Engineering Center for Nanocarbons, Beijing National Laboratory for Molecular Sciences, College of Chemistry and Molecular Engineering, Peking University, Beijing 100871, China

**Yi Cheng** – Center for Nanochemistry, Beijing Science and Engineering Center for Nanocarbons, Beijing National Laboratory for Molecular Sciences, College of Chemistry and Molecular Engineering, Peking University, Beijing 100871, China

**Can Liu** – State Key Laboratory for Mesoscopic Physics, Academy for Advanced Interdisciplinary Studies, School of Physics, Peking University, Beijing 100871, China

**Kewen Huang** – Center for Nanochemistry, Beijing Science and Engineering Center for Nanocarbons, Beijing National Laboratory for Molecular Sciences, College of Chemistry and Molecular Engineering, Peking University, Beijing 100871, China

**Junliang Li** – Beijing Graphene Institute (BGI), Beijing 100095, China

**Puxin Wang** – Department of Biomedical Engineering, Academy for Advanced Interdisciplinary Studies, College of Engineering, Peking University, Beijing 100871, China

**Xiaojie Duan** – Beijing Graphene Institute (BGI), Beijing 100095, China; Department of Biomedical Engineering, Academy for Advanced Interdisciplinary Studies, College of Engineering, Peking University, Beijing 100871, China; [orcid.org/0000-0001-7799-3897](https://orcid.org/0000-0001-7799-3897)

Complete contact information is available at:  
<https://pubs.acs.org/10.1021/acsnano.0c01298>

### Author Contributions

<sup>†</sup>G. Cui, Y. Cheng, and C. Liu contributed equally to this work.

### Notes

The authors declare no competing financial interest.

### ACKNOWLEDGMENTS

This work was financially supported by the National Basic Research Program of China (No. 2016YFA0200103), the National Natural Science Foundation of China (Nos. 51520105003, 51432002, and U1904193), Beijing Graphene Innovation Program (No. Z181100004818003), Beijing Municipal Science & Technology Commission (Nos. Z181100004218006 and Z181100004818001), and Zhongyuan Thousand Talents Program of Henan Province and National Postdoctoral Program for Innovative Talents (No. BX20190016).

### REFERENCES

- (1) Novoselov, K. S.; Geim, A. K.; Morozov, S. V.; Jiang, D.; Zhang, Y.; Dubonos, S. V.; Grigorieva, I. V.; Firsov, A. A. Electric Field Effect in Atomically Thin Carbon Films. *Science* **2004**, *306*, 666–669.
- (2) Novoselov, K. S.; Geim, A. K.; Morozov, S. V.; Jiang, D.; Katsnelson, M. I.; Grigorieva, I. V.; Dubonos, S. V.; Firsov, A. A. Two-Dimensional Gas of Massless Dirac Fermions in Graphene. *Nature* **2005**, *438*, 197–200.
- (3) Nair, R. R.; Blake, P.; Grigorenko, A. N.; Novoselov, K. S.; Booth, T. J.; Stauber, T.; Peres, N. M. R.; Geim, A. K. Fine Structure Constant Defines Visual Transparency of Graphene. *Science* **2008**, *320*, 1308–1308.
- (4) Lee, C.; Wei, X. D.; Kysar, J. W.; Hone, J. Measurement of the Elastic Properties and Intrinsic Strength of Monolayer Graphene. *Science* **2008**, *321*, 385–388.
- (5) Balandin, A. A. Thermal Properties of Graphene and Nanostructured Carbon Materials. *Nat. Mater.* **2011**, *10*, 569–581.
- (6) Mayorov, A. S.; Gorbachev, R. V.; Morozov, S. V.; Britnell, L.; Jalil, R.; Ponomarenko, L. A.; Blake, P.; Novoselov, K. S.; Watanabe, K.; Taniguchi, T.; Geim, A. K. Micrometer-Scale Ballistic Transport in Encapsulated Graphene at Room Temperature. *Nano Lett.* **2011**, *11*, 2396–2399.
- (7) Zhang, Y. B.; Tang, T. T.; Girit, C.; Hao, Z.; Martin, M. C.; Zettl, A.; Crommie, M. F.; Shen, Y. R.; Wang, F. Direct Observation of a Widely Tunable Bandgap in Bilayer Graphene. *Nature* **2009**, *459*, 820–823.
- (8) Kim, K.; Choi, J. Y.; Kim, T.; Cho, S. H.; Chung, H. J. A Role for Graphene in Silicon-Based Semiconductor Devices. *Nature* **2011**, *479*, 338–344.
- (9) Novoselov, K. S.; Fal'ko, V. I.; Colombo, L.; Gellert, P. R.; Schwab, M. G.; Kim, K. A Roadmap for Graphene. *Nature* **2012**, *490*, 192–200.
- (10) Zhang, K.; Zhang, L. L.; Zhao, X. S.; Wu, J. S. Graphene/Polyaniline Nanofiber Composites as Supercapacitor Electrodes. *Chem. Mater.* **2010**, *22*, 1392–1401.
- (11) Chen, W. F.; Li, S. R.; Chen, C. H.; Yan, L. F. Self-Assembly and Embedding of Nanoparticles by *In Situ* Reduced Graphene for Preparation of a 3D Graphene/Nanoparticle Aerogel. *Adv. Mater.* **2011**, *23*, 5679–5683.
- (12) Nair, R. R.; Wu, H. A.; Jayaram, P. N.; Grigorieva, I. V.; Geim, A. K. Unimpeded Permeation of Water through Helium-Leak-Tight Graphene-Based Membranes. *Science* **2012**, *335*, 442–444.
- (13) Xin, G. Q.; Yao, T. K.; Sun, H. T.; Scott, S. M.; Shao, D. L.; Wang, G. K.; Lian, J. Highly Thermally Conductive and Mechanically Strong Graphene Fibers. *Science* **2015**, *349*, 1083–1087.
- (14) Xu, Z.; Liu, Y. J.; Zhao, X. L.; Peng, L.; Sun, H. Y.; Xu, Y.; Ren, X. B.; Jin, C. H.; Xu, P.; Wang, M.; Gao, C. Ultrastiff and Strong Graphene Fibers via Full-Scale Synergetic Defect Engineering. *Adv. Mater.* **2016**, *28*, 6449–6456.
- (15) Serrano-Garcia, W.; Jayathilaka, W. A. D. M.; Chinnappan, A.; Tran, T. Q.; Baskar, C.; Thomas, S. W.; Ramakrishna, S. Nanocomposites for Electronic Applications That Can Be Embedded for Textiles and Wearables. *Sci. China: Technol. Sci.* **2019**, *62*, 895–902.
- (16) Tran, T. Q.; Lee, J. K. Y.; Chinnappan, A.; Loc, N. H.; Tran, L. T.; Ji, D.; Jayathilaka, W. A. D. M.; Kumar, V. V.; Ramakrishna, S. High-Performance Carbon Fiber/Gold/Copper Composite Wires for Lightweight Electrical Cables. *J. Mater. Sci. Technol.* **2020**, *42*, 46–53.
- (17) Xu, Z.; Gao, C. Graphene Chiral Liquid Crystals and Macroscopic Assembled Fibres. *Nat. Commun.* **2011**, *2*, 571.
- (18) Dong, Z. L.; Jiang, C. C.; Cheng, H. H.; Zhao, Y.; Shi, G. Q.; Jiang, L.; Qu, L. T. Facile Fabrication of Light, Flexible and Multifunctional Graphene Fibers. *Adv. Mater.* **2012**, *24*, 1856–1861.
- (19) Cheng, H. H.; Dong, Z. L.; Hu, C. G.; Zhao, Y.; Hu, Y.; Qu, L. T.; Chena, N.; Dai, L. M. Textile Electrodes Woven by Carbon Nanotube-Graphene Hybrid Fibers for Flexible Electrochemical Capacitors. *Nanoscale* **2013**, *5*, 3428–3434.
- (20) Compton, O. C.; Nguyen, S. T. Graphene Oxide, Highly Reduced Graphene Oxide, and Graphene: Versatile Building Blocks for Carbon-Based Materials. *Small* **2010**, *6*, 711–723.
- (21) Feng, L. C.; Chang, Y.; Zhong, J.; Jia, D. C. Dry Spin Graphene Oxide Fibers: Mechanical/Electrical Properties and Microstructure Evolution. *Sci. Rep.* **2018**, *8*, 10803.
- (22) Samad, Y. A.; Li, Y. Q.; Alhassan, S. M.; Liao, K. Non-Destroyable Graphene Cladding on a Range of Textile and Other Fibers and Fiber Mats. *RSC Adv.* **2014**, *4*, 16935–16938.
- (23) Kim, Y. S.; Kang, J. H.; Kim, T.; Jung, Y.; Lee, K.; Oh, J. Y.; Park, J.; Park, C. R. Easy Preparation of Readily Self-Assembled High-Performance Graphene Oxide Fibers. *Chem. Mater.* **2014**, *26*, 5549–5555.
- (24) Pegoretti, A.; Fambri, L.; Zappini, G.; Bianchetti, M. Finite Element Analysis of a Glass Fibre Reinforced Composite Endodontic Post. *Biomaterials* **2002**, *23*, 2667–2682.
- (25) Joseph, S.; Sreekala, M. S.; Oommen, Z.; Koshy, P.; Thomas, S. A Comparison of the Mechanical Properties of Phenol Formaldehyde Composites Reinforced with Banana Fibres and Glass Fibres. *Compos. Sci. Technol.* **2002**, *62*, 1857–1868.
- (26) Bhaviripudi, S.; Jia, X. T.; Dresselhaus, M. S.; Kong, J. Role of Kinetic Factors in Chemical Vapor Deposition Synthesis of Uniform Large Area Graphene Using Copper Catalyst. *Nano Lett.* **2010**, *10*, 4128–4133.
- (27) Li, G.; Huang, S. H.; Li, Z. Y. Gas-Phase Dynamics in Graphene Growth by Chemical Vapor Deposition. *Phys. Chem. Chem. Phys.* **2015**, *17*, 22832–22836.
- (28) Wang, H. P.; Yu, G. Direct CVD Graphene Growth on Semiconductors and Dielectrics for Transfer-Free Device Fabrication. *Adv. Mater.* **2016**, *28*, 4956–4975.
- (29) Chen, X. D.; Chen, Z. L.; Jiang, W. S.; Zhang, C. H.; Sun, J. Y.; Wang, H. H.; Xin, W.; Lin, L.; Priyadarshi, M. K.; Yang, H.; Liu, Z. B.; Tian, J. G.; Zhang, Y. Y.; Zhang, Y. F.; Liu, Z. F. Fast Growth and Broad Applications of 25-Inch Uniform Graphene Glass. *Adv. Mater.* **2017**, *29*, 1603428.
- (30) Chen, J. Y.; Wen, Y. G.; Guo, Y. L.; Wu, B.; Huang, L. P.; Xue, Y. Z.; Geng, D. C.; Wang, D.; Yu, G.; Liu, Y. Q. Oxygen-Aided Synthesis of Polycrystalline Graphene on Silicon Dioxide Substrates. *J. Am. Chem. Soc.* **2011**, *133*, 17548–17551.
- (31) Sun, J. Y.; Chen, Y. B.; Priyadarshi, M. K.; Chen, Z.; Bachmatyuk, A.; Zou, Z. Y.; Chen, Z. L.; Song, X. J.; Gao, Y. F.; Rummeli, M. H.; Zhang, Y. F.; Liu, Z. F. Direct Chemical Vapor Deposition-Derived Graphene Glasses Targeting Wide Ranged Applications. *Nano Lett.* **2015**, *15*, 5846–5854.
- (32) Sun, J. Y.; Zhang, Y. F.; Liu, Z. F. Direct Chemical Vapor Deposition Growth of Graphene on Insulating Substrates. *ChemNanoMat* **2016**, *2*, 9–18.
- (33) Zheng, Y.; Wang, S. B. Effect of Moderately High Temperature Heat Treatment on Surface Morphology and Structure of Quartz Fibers. *Appl. Surf. Sci.* **2012**, *258*, 4698–4701.

(34) Liu, Y.; Zhu, J. X.; Chen, Z. F.; Jiang, Y.; Li, C. D.; Li, B. B.; Lin, L.; Guan, T. R.; Chen, Z. H. Mechanical Properties and Microstructure of 2.5D (Shallow Straight-Joint) Quartz Fibers-Reinforced Silica Composites by Silicasol-Infiltration-Sintering. *Ceram. Int.* **2012**, *38*, 795–800.

(35) Reznik, B.; Guellali, M.; Gerthsen, D.; Oberacker, R.; Hoffmann, W. Microstructure and Mechanical Properties of Carbon-Carbon Composites with Multilayered Pyrocarbon Matrix. *Mater. Lett.* **2002**, *52*, 14–19.

(36) Luo, R. Y.; Cheng, J. W.; Wang, T. M. Oxidation Behavior and Protection of Carbon/Carbon Composites Prepared Using Rapid Directional Diffused CVI Techniques. *Carbon* **2002**, *40*, 1965–1972.

(37) Li, H. J.; Li, A. J.; Bai, R. C.; Li, K. Z. Numerical Simulation of Chemical Vapor Infiltration of Propylene into C/C Composites with Reduced Multi-Step Kinetic Models. *Carbon* **2005**, *43*, 2937–2950.

(38) Schedin, F.; Geim, A. K.; Morozov, S. V.; Hill, E. W.; Blake, P.; Katsnelson, M. I.; Novoselov, K. S. Detection of Individual Gas Molecules Adsorbed on Graphene. *Nat. Mater.* **2007**, *6*, 652–655.

(39) Dan, Y.; Lu, Y.; Kybert, N. J.; Luo, Z.; Johnson, A. T. C. Intrinsic Response of Graphene Vapor Sensors. *Nano Lett.* **2009**, *9*, 1472–1475.

(40) Li, Z.; Xu, Z.; Liu, Y.; Wang, R.; Gao, C. Multifunctional Non-Woven Fabrics of Interfused Graphene Fibres. *Nat. Commun.* **2016**, *7*, 13684.

(41) Meng, F.; Lu, W.; Li, Q.; Byun, J. H.; Oh, Y.; Chou, T. W. Graphene-Based Fibers: A Review. *Adv. Mater.* **2015**, *27*, 5113–5131.